Supplementary Material for

Perching and takeoff of a robotic insect on overhangs using switchable electrostatic adhesion

M. A. Graule,* P. Chirarattananon, S. B. Fuller, N. T. Jafferis, K. Y. Ma, M. Spenko,
R. Kornbluh, R. J. Wood*

*Corresponding author. Email: graule@mit.edu (M.A.G.); rjwood@seas.harvard.edu (R.J.W.)

This PDF file includes:

Materials and Methods
Figs. S1 to S11
Table S1
Full Reference List

Other Supplementary Material for this manuscript includes the following:
(available at www.sciencemag.org/content/352/6288/978/suppl/DC1)

Movie S1

Materials and Methods

1. Robot platform

The insect-scale flying robot at the center of this research effort is a modified version of the vehicle presented in (*23*). In brief, this two-winged, flapping micro air vehicle consists of two custom-built piezoelectric ceramic actuators each driving a single passively rotating wing. The robotøs surrounding mechanical structure and transmission mechanisms are constructed from a laminated carbon fiber composite with polyimide flexure hinges. Its wings consist of carbon fiber frames with a thin polyester membrane. Components are precision machined and fabricated separately before being hand-assembled ó in part using origami-inspired folding ó into the full robot.

The current version of the robot consists of this insect-scale vehicle interfaced with an off-board power source, an external motion capture system, and a flight controller. The design, fabrication, and operation of the vehicle are described in detail in (*23*). Relevant to the discussion below, the robot weighs 84 mg without additional onboard components. It has a wingspan of 36 mm, a body height of 20 mm, and a payload capacity of approximately 50-150mg (depending on the design).

2. Electrostatic adhesives

2.1. Design

The force due to electrostatic adhesion is often assumed to scale linearly with the area of the patch and the permittivity of the dielectric layer, to be proportional to the square of the applied voltage, and to be inversely proportional to the total distance (thickness of dielectric layer and air gap) between the electrodes and the substrate (*15, 25, 27*). However, this neglects effects such as electrode geometry, surface roughness, charge accumulation, leakage currents, and humidity (*19, 25, 28, 29*). For example, it was found that the force in an electrostatic chuck for silicon wafers only scales with the square of the applied voltage until 1100V at ambient conditions (*29*). We therefore deemed it impractical to develop our patch solely based on analytical or numerical models and chose an experimental approach to designing the dimensions of our electrostatic adhesive. The experimentally determined adhesion of a large electrostatic patch with comb-like electrodes (Fig. S3) informed the final size of the circular electroadhesive used in the flight demonstrations. Numerical simulations (section 2.2) indicate that the adhesion pressures for the two patches are comparable despite differences in size and geometry.

Mindful of practical considerations for the insect-scale vehicle, 1000V was chosen as the operating voltage limit for our adhesive patches. Powering the patch with onboard components will be an important requirement once the vehicle becomes untethered. We have previously presented a lightweight tapped inductor boost converter as a solution to stepping up a battery voltage (~3V) to 200-300V, weighing only ~20mg (*30*). Combining a similar boost converter with a charge pump ladder stage would enable the generation of 1000V onboard a future prototype. Higher voltages would potentially allow for a smaller patch size, but require heavier and less efficient power electronics and greater insulation of all onboard wire connections, making integration more challenging. As the weight of the presented patch (~6mg) is significantly lower than the expected weight of the power

electronics, increasing to supply voltage to decrease its size would have diminishing returns. Alternatively, the vehicle payload can support an increased patch size with even lower voltages to maintain the required adhesive force, however there are again diminishing returns since larger patches could begin to interfere with the aerodynamics of the vehicle.

2.2. Modeling

Simulations of the electrostatic force were performed in COMSOL Multiphysics 5.1 (COMSOL AB, Stockholm, Sweden) for both rectangular and circular electrode geometries. According to our simulations, for an interdigitated or concentric circle pattern, smaller gap sizes result in higher electrostatic forces. We designed for the minimum gap size possible considering manufacturing limitations, such as the resolution of our masking in copper deposition. The width of the electrodes depends on the expected distance between the adhesive and substrate. The greater the distance, the larger the electrode widths. This distance can be used as a proxy for roughness. As such, rougher substrates demand wider electrodes. The simulated normal adhesion pressures for both electrodes on glass and wood for an average air gap (between substrate and polyimide) of 20 m and 50 m respectively are presented in Table S1. The simulated adhesion pressures for the circular patch reach ~80% of the pressures calculated for the comb-like electrode pattern.

2.3. Fabrication

Our fabrication method was key to producing patches of sufficient adhesion pressure that are light enough to be carried by the flapping-wing microrobot. A major weight reduction was achieved through sputter-coating the copper electrodes, which allowed us to manufacture flexible electrodes with a thickness of less than 200nm. The fabrication process is depicted in Fig. S2. The electrode geometries of the test patch for characterization and the circular patch are shown in Fig. S3. A scanning electron microscope (SEM) image of the cross section of the final patch is shown in Fig. S1. The test patch had a total area of 19.32 cm^2 and weighed 58 mg. The circular patch had a total area of 1.7 cm^2 (excluding tabs to connect power supply wires) and weighed 6 mg.

2.4. Experimental characterization

2.4.1. Normal adhesion pressure measurements

The normal adhesion achievable with a test patch with the comb-like electrode geometry shown in Fig. S3 was determined as follows: The patch was mounted on a rigid holder as depicted in Fig. S4 and a cord was used to connect the holder to a 10 N static load cell (Serial No. 100282) in an Instron Material Tester (Model 5544A, Instron, Norwood, MA 02062, USA). Five measurements each at 1000V were conducted on glass, steel (polished, untreated, and sandblasted), copper, unfinished plywood, red brick, and glass again in ambient air (relative humidity 59-70%). Neither patch nor substrates were cleaned between measurements. The patch was also not cleaned when the substrates were switched. Each measurement followed the same protocol: the patch was brought into contact with the substrate such that its weight was not supported by the cord. The voltage was then switched on, followed by a 60s waiting period. Then, the tension on the string was gradually increased (commanded rate 4N/min) until detachment. The adhesion

3

forces reported were obtained as the difference between the peak tension before detachment and the force measured after detachment (weight of the mount and patch). Power was supplied to the patch via ultra-thin insulated copper wires (52 AWG; product code 52TPN-155 Red, MWS Wire Industries, Westlake Village, CA 91362, USA) to avoid the effect of wire stiffness on the measurements. We waited at least six minutes between measurements to allow the substrate and patch to return to their initial electric states (e.g. no trapped charges).

2.4.2. Effect of humidity on adhesion pressure

Prior studies have shown that electrostatic force generation is affected by humidity (*28, 29, 31-33*). Adhesion pressures between an electrostatic chuck (sapphire dielectric, 2500V) and a silicon wafer were reported to drop by a factor of ~1.5 when going from dry nitrogen to ambient air at 63% relative humidity (RH); and a factor of ~2 from ambient air with an additional thin condensation layer (*28*). Similarly, a roughly threefold decrease in adhesion pressure in humid air was found for an electrostatic clamp for silicon wafers at a voltage of 1500V ó the decrease in pressure for humid air was less pronounced at lower voltages (*29*). The retention pressure of an alumina electrostatic chuck for silicon wafers (200-1600V) was reported to be twice as strong at 35%RH than at 65%RH (*31*). The top speed of an electrostatically driven glass disc (400V), which is proportional to the maximum achievable lateral forces, was presented to peak at 25%RH and decrease by a factor of ~2 when the relative humidity is increased to 50% (*32*). Furthermore, the forces of an electrostatic microscale actuator with Si_3N_4 as the dielectric material were found to drop by a factor of ~3 when the relative humidity is increased from 35% - 50% (*33*). From these previous studies across a range of materials, we can conclude that humidity can reduce electrostatic adhesion pressure by a factor of approximately 1.5-3. However, one important difference between these previous studies and the presented electroadhesive patch is the relative compliance: these previous tests were done with rigid structures while the patch described here is designed to be compliant in order to conform to non-planar surfaces. More discussion of the relevance of this quality is described below.

Wood and red brick, unlike the materials discussed above, are porous and can absorb water. We expect that humidity can actually enhance electroadhesion for surfaces like wood due to the increased conductivity of the surface, thus a greater electric field can be established between the electrodes and the surface. To explore this effect we complement the above discussion by characterizing the effect of relative humidity on the adhesion pressure on plywood. For this purpose, we enclosed our setup with two commercial desktop humidifiers to control the humidity. Adhesion tests as described in section 2.4.1. were then performed at different values of relative humidity. The mounting approach was adjusted slightly to facilitate patch mounting and removal by adding Gel-Pak Grade 4 (Delphon, Hayward, California, United States) between the posts and the patch. The results shown in Fig. S7 indicate that the adhesion of our patch on plywood increases with increasing humidity, in this case by a factor of approximately two.

Finally, humidity can have additional effects when the materials in contact are extremely flat and/or hydrophilic, further enhancing the electrostatic pressure. For example, on glass and polished metal, high humidity can form a water layer on the surface that can interact with the patch through surface tension forces. Similarly, a water

layer could form a seal around the perimeter of the patch that could cause a suction effect. Both of these would be enhanced or engaged by activating the electroadhesive. These effects are partially due to the thin and compliant nature of these adhesive patches. Humidity could also form a microlayer of moisture to effectively make it more conductive, in a similar manner as described above for wood. Finally, one of the dielectric materials could be absorbing the moisture and effectively increasing the clamping force due to Johnsen-Rahbek effects (in which the more conductive dielectric has a lower voltage drop across it resulting in a higher voltage drop across the air interface). We believe that a subset or aggregate of these effects are the cause of larger standard deviations in our previous tests on smooth surfaces, but are not present on porous or rougher surfaces.

Regardless of the detailed mechanisms involving humidity (or other variables that couple impact adhesive pressure), our experimental approach allows us to characterize adhesion and then choose a patch geometry that will enable perching with some factor of safety relative to the worst case that we observed. In addition, these humidity/moisture-dependent effects could have a negative impact on detachment. However, these can be easily mitigated when designing the adhesive patch: the patch surface can be made hydrophobic and the patch can be made porous or have air paths to eliminate any suction effects.

2.4.3. Effect of surface roughness on normal adhesion

The surface profile of our substrates was determined using a LEXT 3D Measuring Laser Microscope (OLS4000, Olympus, Shinjuku, Tokyo, Japan). For each of the materials, the surface profile was acquired at three randomly selected spots over an area of 5233μm x 5185μm, resulting in profile data containing 1024 x 1025 discrete points. This data was filtered with a moving average filter (size 301 x 301, corresponding to 1.54mm x 1.52mm), and the filtered data was subtracted from the original data to discount the effect of variations in form (as defined in Fig. S6) when calculating the roughness for each sample spot (arithmetic average of absolute values). The roughness values S_a as reported in Fig. 2(A) were obtained by averaging the roughness values calculated from the three sample spots per material.

In order to identify how the adhesion of our electroadhesives is affected by surface roughness, three steel samples with different surface profiles were prepared: the surface of one sample remained untreated (S_a = 84.4 m), one was sandblasted (grain material: AlO, grain diameter: Ö250μm; resulting S_a = 75.3 m), and one was polished using a conventional belt sander (grit: 60; resulting S_a = 54.6 m). The resulting normal adhesion pressures for the different steel surfaces are shown in Fig. 2A. It is evident that the parameter S_a does not explain the varying adhesive strengths on the three steel samples (untreated: adhesion 153.8Pa, S_a = 84.4 m; sandblasted: adhesion 102.7Pa, S_a = 75.3 m; belt sander: adhesion 205.9Pa, S_a = 54.6 m). However, if the data is corrected for form and low-frequency waviness (by applying Gaussian blur with size 801 x 801 (4.09mm x 4.05mm) to it and subtracting this from the original data to obtain the filtered data), a smaller standard deviation in the height distribution (Fig. S5) correlates with higher normal adhesion. A possible explanation for this is that the high flexibility of the presented electroadhesives allows them to conform to low-frequency changes in profile height (Fig. S6(B)). Since they cannot conform to high-frequency roughness, a broader

height distribution after low-frequency correction corresponds to a higher average air gap between electrodes and substrate, which in turn results in lower adhesive pressure. Similarly, we expect that a higher adhesion pressure can be achieved on profiles with negative skewness R_{sk} (i.e. the profile height distribution is skewed such that pits are more likely than bumps; see Fig. S6(C)).

It is worth noting that the cut-off wavelength used in the filtering described above is in the same order of magnitude as the width of the copper electrodes. The copper electrodes are significantly stiffer than the surrounding insulating materials. It is therefore likely that the patch conforms better to profile changes with a characteristic length larger than the electrode width.

2.4.4. Power requirement of the patch used in perching experiments

In order to determine the leakage and charging currents of the final patch on unfinished plywood, glass and copper, the patch was placed onto each of the substrates and connected to an oscilloscope (Tektronix TDS 2014B, Tektronix, Beaverton, OR 97077, USA) measuring the voltage drop over a known resistance ($RS = 10M\Omega$) according to the schematic shown in Fig. S8. This voltage drop was recorded for a time window around the switching time (t = 0). The leakage current was calculated as the time average of the current data after the current reaches steady state. The relative humidity was 63% during these experiments.

We found the power requirement of the patch to be below 7µW for the tested materials. For comparison, the flight power of our insect-scale vehicle without a payload is 19mW (*23*).

2.5. Flight experiments

The flight controller architecture used in the perching and detachment maneuvers relies on a logic module that detects relevant events to initiate a landing attempt or recognize a successful attachment. This module adjusts the reference position to initiate different maneuvers, which is then fed into the adaptive blocks controlling altitude, latitude and attitude (*23*). A controller block diagram is provided in Fig. S9 to illustrate the controller logic.

The flight experiments were conducted using the setup and control approach as described in (*23*). The controller gains were adjusted to account for the change in dynamics caused by mounting a weight (i.e. the patch) on top of the microrobot.

The adjusted model parameters and controller gains were found by trimming flights on a tether. For this purpose, the patch and mount allow for the attachment of a carbon fiber rod (weight <1mg) as shown in Fig. S11, which in turn was fixed to a Kevlar thread to hang the robot upright. The rigid rod was used to reduce the risk of the Kevlar being entangled in the wings. The effect of the rod and the tether on the vehicle dynamics were negligible. Once the trimming flights provided sufficient information to understand the dynamics of the robot and tune the controller gains, the carbon fiber rod and the thread were removed.

During the perching experiment series, one failed perching attempt occurred with a natural leaf test. This failed attempt can be entirely attributed to the occlusion of the robot's tracking markers from the tracking cameras that provide the robot's state

feedback. The controller is programmed to switch off all actuation as soon as the robot is occluded to avoid severe crashes where an actuated wing impacts the ground or other rigid objects. With eventual power and control autonomy implemented on the robot, state estimation will be performed onboard, and this failure mode will be less likely to occur.

Engagement and disengagement of the electrostatic adhesive patch is modulated by binary switching of a 1000V signal. Residual charges do remain during disengagement, leading to residual adhesion. The level of residual adhesion varies with the surface material. To characterize the detachment time constant, we attached an energized circular patch with 84mg dummy weight to the underside of brick, glass and plywood (5 times each); switched off the voltage; and waited for detachment caused by the dummy weight. Detachment from glass and brick occurred nearly instantaneously; detachment from wood occurred within a 1-5s after removing power from the patch.

To account for residual adhesion during detachment, we programmed the flight control logic to perform the following protocol: 1) Set the reference height of the robot to be at the perched position and start up the robotøs wings to fully support the robotøs weight. 2) After one second, de-energize the adhesive patch. Continue attempting to maintain the perching altitude for seven seconds after the de-energizing event. This provides time for residual charges to dissipate at the adhesive interface. 3) Gradually decrease the reference height to a position slightly below the ceiling. If adhesion between substrate and patch remains at this stage, the adaptive part of the controller will lead to a continuous decrease in lift, until the robotøs weight results in disengagement. 4) After disengagement, hover a few centimeters below the perching surface, then descend and land.

3. Insect-scale flapping-wing flight in ceiling proximity

3.1. Experimental characterization

The effect of the presence of a ceiling on the robotøs lift force was determined as follows: The robot was glued to a custom-built capacitive force sensor that measures force in the lift direction (*34*). A flat plate was positioned perpendicularly to the lift direction, and mounted on a micrometer stage to allow the lift force to be measured for various distances between the plate and the leading edge of the wings (see Fig. S10(A)). To control for the possibility of robot degradation over the course of the experiment, the lift forces were measured in different orders: first with no plate, then with the plate increasing its distance from the robot, then no plate, then decreasing distance, then no plate, then increasing distance, and then no plate again. For each gap distance tested, the robot was flapped for one second (greater than 100 wing beat periods), and the mean value of the lift force over this time was recorded. For a given distance, the lift force was computed as the arithmetic mean of these measurements. The normalized lift was obtained by dividing this value by the arithmetic mean of the unaffected lift data (no plate). The results (Fig. S10(A)) show that the lift force is increased by about 46% when the plate is 1.79 mm away from the ceiling, while this lift-enhancement drops to less than 6% once the gap is greater than 10 mm.

3.2. Theoretical stability analysis

To understand the dynamics of the robot at the instance it encounters the ceiling, we use a physics-based, simplified dynamical model that describes the translational and rotational dynamics of the robot. The landing maneuver is divided into two primary stages. The first stage is when the robot comes into the proximity of the ceiling and is influenced by the increased lift from the ceiling effect; at this stage, no part of the robot is in direct contact with the ceiling. The second stage is when the robot is partially in contact with the ceiling and the electro-adhesive anchor starts to affects the dynamics of the robot.

To begin, we consider the robot in free flight (Fig. S10(B)). For the sake of simplicity, we only consider the dynamics of the robot in a 2D plane. For a robot of mass m and moment of inertia I flying at distance d from the ceiling, with the tilt angle θ, we can write the equations of motion for the altitude and rotational dynamics as

$$I\ddot{\theta} = \left(F_2 - F_1\right)l$$
$$m\ddot{d} = mg - \left(F_1 + F_2\right)\cos\theta,$$

where F_1 and F_2 are instantaneous forces generated by two wings and l is the distance from the center of mass to the center of pressure along the body pitch axis. Because the two wings are at different distances from the ceiling, they nominally produce unequal amounts of lift. Modeling the ceiling effect to be a function of the distance from the wing to the ceiling, we may write

$$F_1 = F_{commanded}\left(1 + \lambda d_1^{-1}\right)$$
$$F_2 = F_{commanded}\left(1 + \lambda d_2^{-1}\right),$$

with $F_{commanded}$ being the commanded force to the robot, nominally equal to $\frac{1}{2}mg$, λ is a fitting parameter, and d_1, d_2 are the distances from the wings to the ceiling, approximately given by $d_1 = d + l\sin\theta$ and $d_2 = d - l\sin\theta$. Combining the results and applying the small angle approximation for the scenario where the robot is only slightly away from the equilibrium condition, we obtain

$$\ddot{\theta} = \frac{\lambda mgl^2}{Id^2}\theta \qquad \text{and} \qquad \ddot{d} = -\lambda g\cos\theta\frac{1}{d}.$$

This suggests that the rotational dynamics near the ceiling are inherently unstable with the degree of instability increasing as the robot approaches the ceiling. Similarly, the altitude dynamics are affected, and the robot is attracted towards the ceiling due to the increase in lift.

Consider the example where the robot is hovering approximately one centimeter away from the ceiling ($d = 1\,\text{cm}$), with a tilt angle of 5 degrees. This results in a torque induced by the ceiling effect of approximately 0.2 Nm when choosing $\lambda \approx 1\text{mm}$ (based on our experimental results). This torque is comparable to the torque generally required for flight control, which is in the order of 0.1 - 1 Nm (23). The analysis here suggests that,

while the attitude dynamics are disturbed by the presence of the ceiling, the disturbance can be corrected by the flight controller. This is supported by the fact that the robot could repeatedly perch on the ceiling without the need to modify the existing flight controller.

Regarding the altitude dynamics, the distance of $d = 1$ cm would result in an acceleration of 0.6ms^{-2} towards the ceiling. At this magnitude of acceleration, it would take the robot less than 200ms for the robot to hit the ceiling. The amount of acceleration is generally much greater than the variation of thrust produced by the robot during altitude control. This suggests that it would effectively attract the robot towards the ceiling and that this effect could not be prevented by flight control.

In the case where the robot contacts the ceiling (Fig. S10(C)), we treat the contact point as a momentarily fixed pivot in the analysis of the subsequent rotational dynamics of the robot (assuming no slip at the contact point). We can then apply a similar analysis as presented above, starting from the equation of motion as

$$\left[I + m\left(H^2 + \frac{D^2}{4}\right)\right]\ddot{\theta} = F_2\left(l - \frac{D}{2}\right) - F_1\left(l + \frac{D}{2}\right) + mg\left(\frac{D}{2}\cos\theta - H\sin\theta\right) + \tau_a.$$

Here, D is the adhesive patch diameter, H is the distance between the center of mass to the top of the patch as defined in Fig. S10(C), and τ_a is the torque from the electrostatic attraction between patch and ceiling (most likely negligibly small). Using the same expressions for F_1 and F_2 as above and applying the small angle approximation, we obtain

$$\left[I + m\left(H^2 + \frac{D^2}{4}\right)\right]\ddot{\theta} \approx \frac{\lambda mgl^2}{d^2}\theta - mgD\left(1 + \frac{\lambda}{d}\right) + mg\left(\frac{D}{2} - H\theta\right) + \tau_a$$

$$\approx mg\left(\frac{\lambda l^2}{d^2} - H\right)\theta - mgD\left(\frac{1}{2} + \frac{\lambda}{d}\right) + \tau_a.$$

To evaluate whether the robot would be attracted to the ceiling, or whether θ would decrease, we are interested in the sign of $\ddot{\theta}$. For a small angle deviation, d becomes the distance from the wing to the top of the adhesive patch, roughly equal to the height of the patch or ≈ 6 mm. Taking $l \approx 10$ mm, $H \approx 10$ mm and $\lambda \approx 1$ mm (a conservative estimate based on our experimental data), we find $H \approx 4\frac{\lambda l^2}{d^2}$. Together with the fact that τ_a would tend to reduce θ, we can confidently conclude that upon making contact, the robot would passively rotate to improve the alignment between patch and ceiling.

200 nm | Width = 8.026 µm | EHT = 5.00 kV | | Signal A = InLens
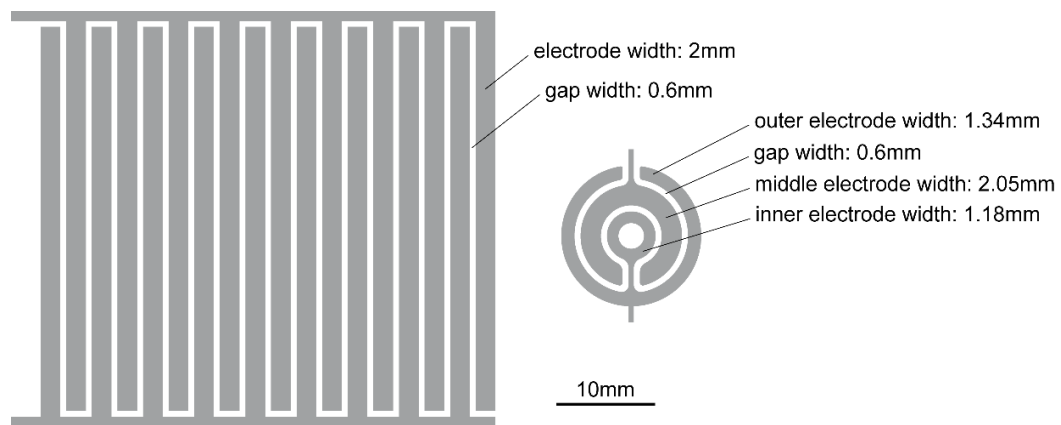Mag = 37.37 K X | WD = 3.5 mm | Sample ID =
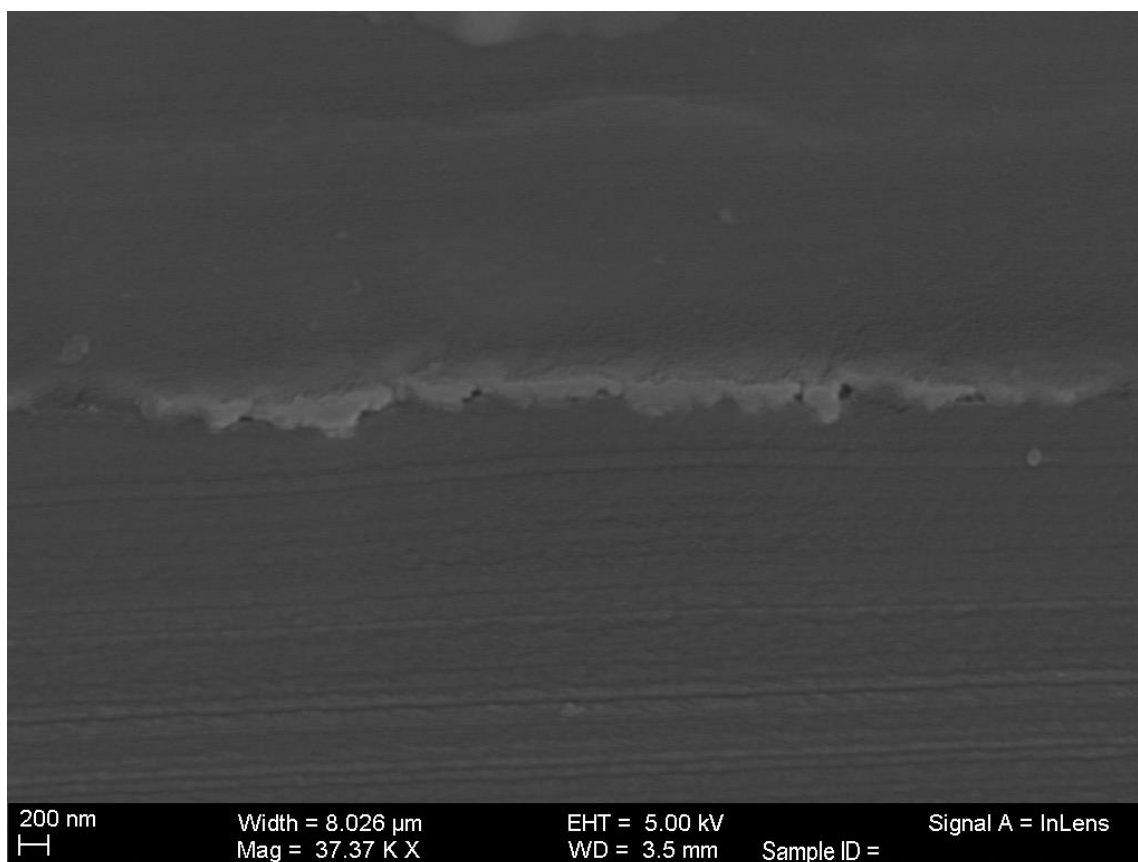
Fig. S1. Cross section of electrostatic adhesive patch.

An SEM image of the cross section of the final patch showing the thicknesses of the copper electrodes.
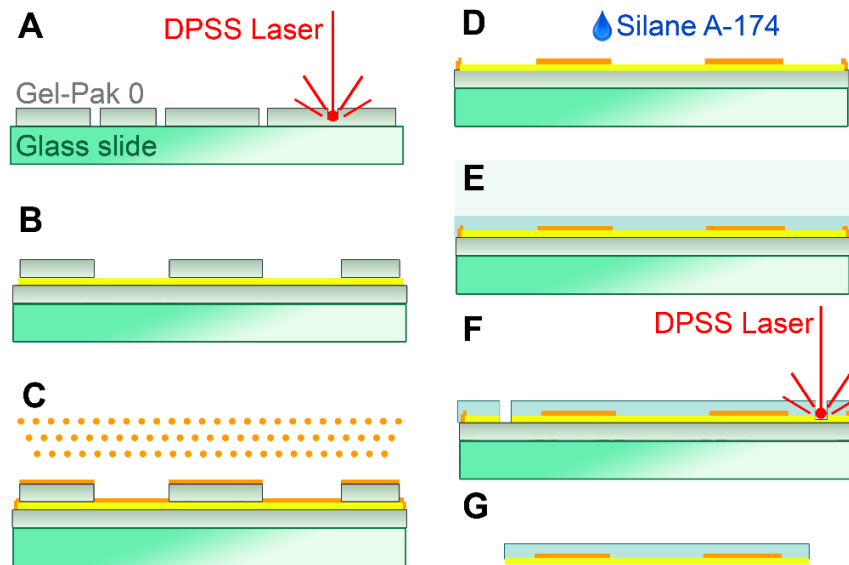
Fig. S2. Fabrication of flexible electroadhesives.

(**A**) The mask for sputter coating the desired geometry is cut from Gel-Pak Grade 0 (Delphon, Hayward, California, United States) with a diode-pumped solid-state (DPSS) laser. (**B**) The Gel-Pak mask is transferred onto a polyimide film (thickness: 12.7µm; supplier: DuPont, Wilmington, Delaware, USA), which is mounted onto a glass slide for support using Gel-Pak 0. (**C**) The copper electrodes are sputter-coated onto the polyimide film (resulting thickness less than 200nm) using a Denton Vacuum Desktop Pro sputter deposition system (Denton Vacuum, LLC, Moorestown, NJ 08057, USA). (**D**) After removing the mask, the sample is treated with Silane A-174 (γ-Methacryloxypropyltrimethoxysilane, Specialty Coating Systems, Indianapolis, IN 46278, USA) as an adhesion primer. (**E**) The sample is coated with Parylene C (thickness: ~10µm; supplier: Specialty Coating Systems) in a chemical vapor deposition chamber (PDS 2010, Specialty Coating Systems). (**F**) The patch is released from the surrounding material with a DPSS laser. (**G**) The resulting patch after it is removed from the glass backing.

electrode width: 2mm

gap width: 0.6mm

outer electrode width: 1.34mm

gap width: 0.6mm

middle electrode width: 2.05mm

inner electrode width: 1.18mm

10mm

Fig. S3. Electrode geometries.

The electrode geometries of the test patch (left) and the final patch (right).
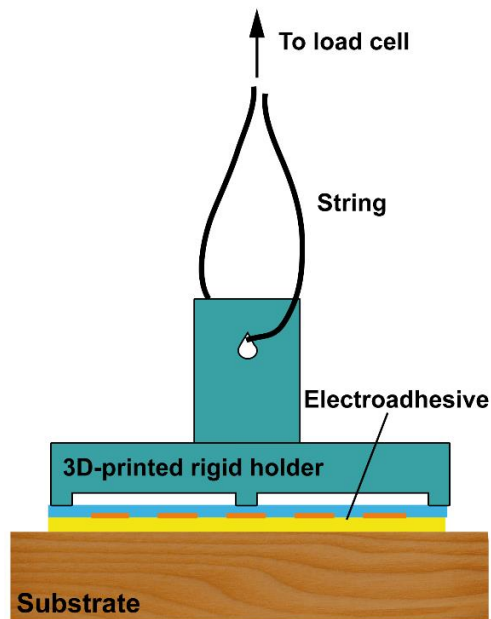
Fig. S4. Setup for adhesion experiments.

The electroadhesive is mounted onto a rigid holding frame (glued to three parallel rectangular ridges as shown) that allows it to conform to the substrate between these posts. The holding frame is connected to the Instron load cell through a flexible cord to ensure that the load transferred onto the electrostatic patch during the adhesion tests is normal to the substrate surface. The substrate was rigidly mounted to the Instron frame.
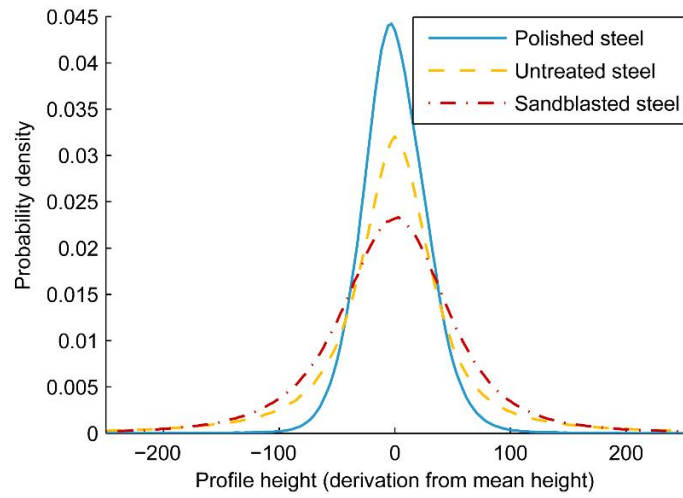
Fig. S5. Profile height distribution for the steel samples used to characterize the effect of roughness on electrostatic adhesion pressure.

The plot shows the height distribution of the surface roughness around the mean height (after correcting for form and waviness). The standard deviation of the distribution correlates with the adhesion pressures obtained from the characterization experiments (see also Fig. 2(A)). A broader distribution is associated with lower adhesion.
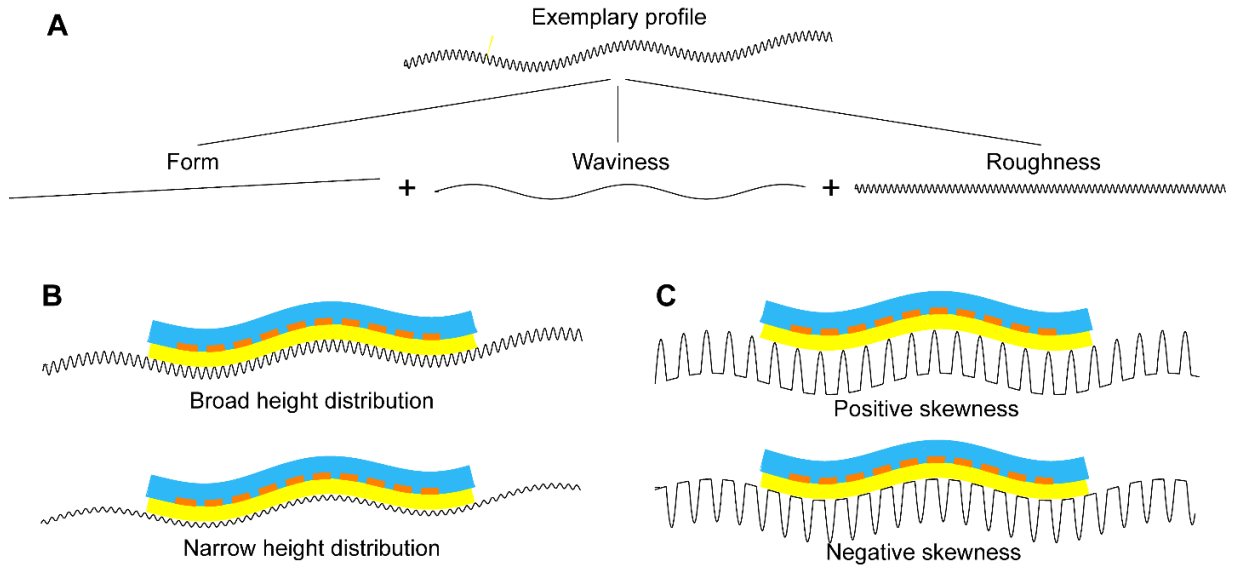
Fig. S6. Compliance of the flexible electroadhesive and the effect of surface roughness.

(**A**) An arbitrary profile can be split into its form (low frequency), waviness (medium frequency) and roughness (high frequency) components. The separation frequencies in this classification are not rigidly defined and depend on the sample of interest. (**B**) The herein presented flexile electrode patch can conform to form and waviness components of a profile, but not to its roughness. Thus, a broader roughness distribution results in an increased average distance between electrodes and substrate, leading to reduced adhesion. (**C**) For identical values of S_a, a profile with positive skewness leads to higher average distance between electrodes and substrate than a profile with negative skewness. Therefore, higher adhesion pressures can be achieved on profiles with negative skewness.
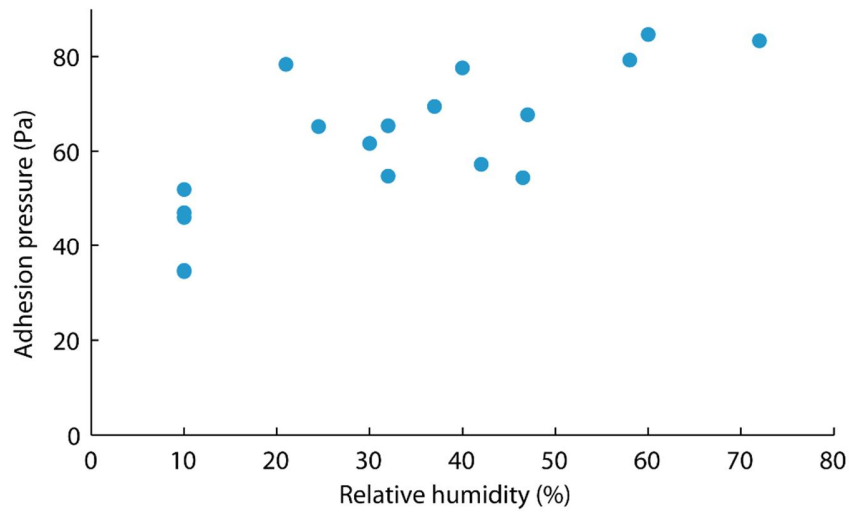
Fig. S7: The effect of relative humidity on electrostatic adhesion on wood.
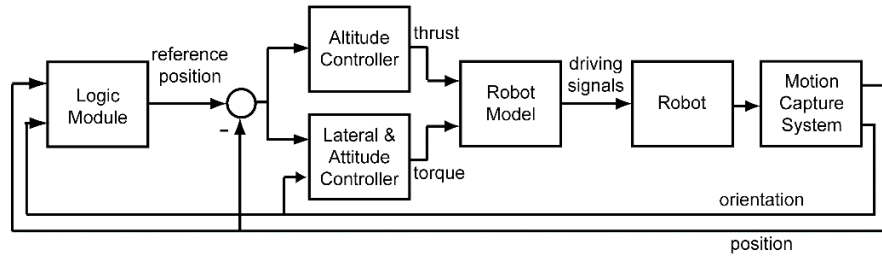
The data suggests that the electrostatic adhesion pressure achievable with the presented patch on plywood increases with increasing relative humidity.
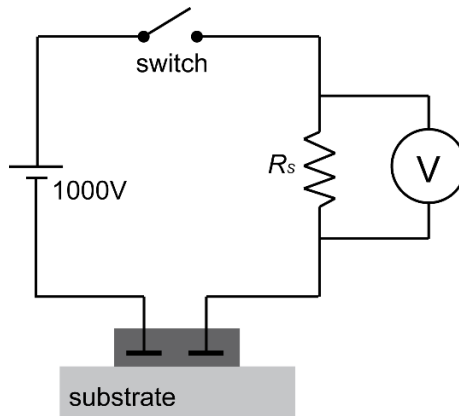
Fig. S8: Current measurement setup.

The setup to measure leakage and charging currents relies on a voltmeter measuring the voltage drop over a shunt resistance R_{S}=10MΩ .

Fig. S9. Flight controller description block diagram.

The robot's position and orientation information is tracked in real-time by an offboard motion capture system. The data is sent to an offboard flight controller, which calculates the thrust and torque necessary to achieve the desired reference flight trajectory. Finally, the thrust and torque values are translated to corresponding actuator driving signals which are sent to the robot through wire tethers. More details are provided in (*23*).
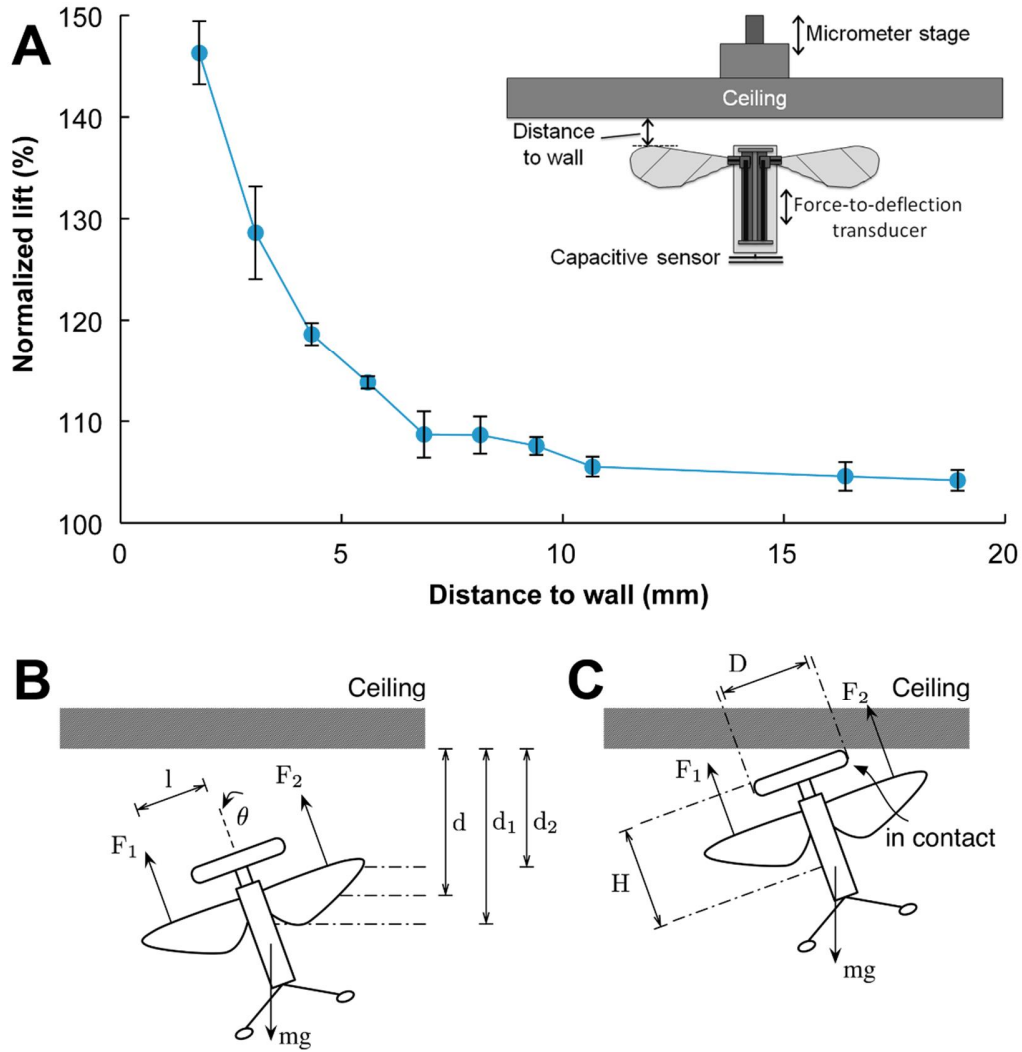
Fig. S10: Flight stability in wall proximity.

(A) Experimentally determined normalized mean lift force as a function of the distance between the leading edge of the wings and an adjustable ceiling plate (average from three measurements per data point). Error bars indicate one standard deviation from three measurements. (Inset: diagram showing the experimental setup). **(B,C)** Sketches denoting the relevant definitions for the stability analysis in ceiling proximity and ceiling contact.

Fig. S11: Tethered trimming of controller parameters.

The electroadhesive patch and the conformal mount allow for the mounting of a carbon fiber rod, which was used to hang the microrobot onto a thin Kevlar tether. This enabled crash-free test flights with varying controller parameters to inform the gains in the final controller used in our flight experiments.

Substrate (relative permittivity)	Air gap (μm)	Adhesion, comb-like electrodes (Pa)	Adesion, circular electrodes (Pa)
Wood (2)	20	41.1	33.2
Wood (2)	50	29.9	24.2
Glass (5)	20	205.6	164.4
Glass (5)	50	128.9	102.4

Table S1: Simulated adhesion pressures.

The electrostatic adhesion pressures were simulated in COMSOL Multiphysics 5.1 for both electrode geometries shown in Fig. S3 on wood and glass for air gap widths of 20 μm and 50 μm.

Movie S1. Successful perching and takeoff demonstrations with an insect-like aerial robot.

This video shows successful perching on plywood, glass and a natural leaf in real-time, followed by a segment showing the landing on a leaf played back at 0.125x real-time speed. The last segment shows two takeoffs to stable hovering flight from plywood, the first played back at real-time speed and the second played back at 0.125x real-time speed. A US quarter dollar is shown for scale.

References and Notes

1. D. Floreano, R. J. Wood, Science, technology and the future of small autonomous drones. *Nature* **521**, 460–466 (2015). Medline doi:10.1038/nature14542

2. M. Tschapka, Pollination of the understorey palm *Calyptrogyne ghiesbreghtiana* by hovering and perching bats. *Biol. J. Linn. Soc. Lond.* **80**, 281–288 (2003). doi:10.1046/j.1095-8312.2003.00235.x

3. B. Anderson, W. W. Cole, S. C. H. Barrett, Botany: Specialized bird perch aids cross-pollination. *Nature* **435**, 41–42 (2005). Medline doi:10.1038/435041a

4. M. Sazima, I. Sazima, The perching bird Coereba flaveola as a co-pollinator of bromeliad flowers in southeastern Brazil. *Can. J. Zool.* **77**, 47–51 (1999). doi:10.1139/cjz-77-1-47

5. C. E. Doyle, J. J. Bird, T. A. Isom, J. C. Kallman, D. F. Bareiss, D. J. Dunlop, R. J. King, J. J. Abbott, M. A. Minor, An avian-inspired passive mechanism for quadrotor perching. *IEEE/ASME Trans. Mechatron.* **18**, 506–517 (2013). doi:10.1109/TMECH.2012.2211081

6. E. W. Hawkes *et al.*, "Dynamic surface grasping with directional adhesion," 2013 IEEE/RSJ International Conference on Intelligent Robots and Systems (IROS), pp. 5487–5493 (2013).

7. J. F. Roberts, J. C. Zufferey, D. Floreano, "Energy management for indoor hovering robots," 2008 IEEE/RSJ International Conference on Intelligent Robots and Systems (IROS), vols 1–3, Conference Proceedings, pp. 1242–1247 (2008).

8. L. Daler, A. Klaptocz, A. Briod, M. Sitti, D. Floreano, "A perching mechanism for flying robots using a fibre-based adhesive," 2013 IEEE International Conference on Robotics and Automation (ICRA), pp. 4433-4438 (2013).

9. D. Mellinger, M. Shomin, V. Kumar, Control of quadrotors for robust perching and landing. *Proc. Int. Power. Lift Conf.* **2010**, 205–225 (2010).

10. M. Kovač, J. Germann, C. Hürzeler, R. Y. Siegwart, D. Floreano, A perching mechanism for micro aerial vehicles. *J. Micro-Nano Mech.* **5**, 77–91 (2009). doi:10.1007/s12213-010-0026-1

11. A. Lussier Desbiens, A. Asbeck, M. Cutkosky, Landing, perching and taking off from vertical surfaces. *Int. J. Robot. Res.* **30**, 355–370 (2011). doi:10.1177/0278364910393286

12. R. Cory, R. Tedrake, Experiments in fixed-wing UAV perching. *Proc. AIAA Guid. Nav. Contr. Conf.* **2008**, 1–12 (2008).

13. A. Frank, J. McGrew, M. Valenti, D. Levine, J. P. How, *Hover, Transition, and Level Flight Control Design for a Single-Propeller Indoor Airplane* (Defense Technical Information Center, 2007).

14. M. L. Anderson *et al.*, "The sticky-pad plane and other innovative concepts for perching uavs," 47th AIAA Aerospace Sciences Meeting (2009).

15. G. J. Monkman, An analysis of astrictive prehension. *Int. J. Robot. Res.* **16**, 1–10 (1997). doi:10.1177/027836499701600101

16. J. P. D. Téllez, J. Krahn, C. Menon, "Characterization of electro-adhesives for robotic applications," 2011 IEEE International Conference on Robotics and Biomimetics (ROBIO), pp. 1867–1872 (2011).

17. H. Prahlad, R. Pelrine, S. Stanford, J. Marlow, R. Kornbluh, "Electroadhesive robots—Wall climbing robots enabled by a novel, robust, and electrically controllable adhesion technology," 2008 IEEE International Conference on Robotics and Automation (ICRA), pp. 3028–3033 (2008).

18. R. Liu, R. Chen, H. Shen, R. Zhang, Wall climbing robot using electrostatic adhesion force generated by flexible interdigital electrodes. *Int. J. Adv. Robot. Syst.* **10**, 36 (2013).

19. R. Chen, R. Liu, H. Shen, "Modeling and analysis of electric field and electrostatic adhesion force generated by interdigital electrodes for wall climbing robots," 2013 IEEE/RSJ International Conference on Intelligent Robots and Systems (IROS), pp. 2327–2332 (2013).

20. H. Wang, A. Yamamoto, T. Higuchi, "Electrostatic-motor-driven electroadhesive robot," 2012 IEEE/RSJ International Conference on Intelligent Robots and Systems (IROS), pp. 914–919 (2012).

21. D. Ruffatto 3rd, A. Parness, M. Spenko, Improving controllable adhesion on both rough and smooth surfaces with a hybrid electrostatic/gecko-like adhesive. *J. R. Soc. Interface* **11**, 20131089 (2014). Medline doi:10.1098/rsif.2013.1089

22. L. Wang, L. Graber, F. Iida, Large-payload climbing in complex vertical environments using thermoplastic adhesive bonds. *IEEE Trans. Robot.* **29**, 863–874 (2013). doi:10.1109/TRO.2013.2256312

23. K. Y. Ma, P. Chirarattananon, S. B. Fuller, R. J. Wood, Controlled flight of a biologically inspired, insect-scale robot. *Science* **340**, 603–607 (2013). Medline doi:10.1126/science.1231806

24. Materials and methods are aviable as supplementary materials on *Science* Online.

25. M. R. Sogard, A. R. Mikkelson, M. Nataraju, K. T. Turner, R. L. Engelstad, Analysis of Coulomb and Johnsen-Rahbek electrostatic chuck performance for extreme ultraviolet lithography. *J. Vac. Sci. Technol. B* **25**, 2155–2161 (2007). doi:10.1116/1.2798724

26. E. Baird, N. Boeddeker, M. R. Ibbotson, M. V. Srinivasan, A universal strategy for visually guided landing. *Proc. Natl. Acad. Sci. U.S.A.* **110**, 18686–18691 (2013). Medline doi:10.1073/pnas.1314311110

27. J. Germann, B. Schubert, D. Floreano, "Stretchable electroadhesion for soft robots," 2014 IEEE/RSJ International Conference on Intelligent Robots and Systems (IROS), pp. 3933–3938 (2014).

28. G. Kalkowski, S. Risse, V. Guyenot, Electrostatic chuck behaviour at ambient conditions. *Microelectron. Eng.* **61-62**, 357–361 (2002). doi:10.1016/S0167-9317(02)00501-4

29. J. van Elp, P. T. M. Giesen, A. M. M. de Groof, Low-thermal expansion electrostatic chuck materials and clamp mechanisms in vacuum and air. *Microelectron. Eng.* **73-74**, 941–947 (2004). doi:10.1016/S0167-9317(04)00248-5

30. M. Karpelson, J. P. Whitney, G. Y. Wei, R. J. Wood, Design and fabrication of ultralight high-voltage power circuits for flapping-wing robotic insects. *Appl. Power Electron. Conf.* **2011**, 2070–2077 (2011).

31. K. J. Jeong, S. Spoutai, S. H. Choi, T. Y. Cho, H. G. Chun, A study on the fabrication and characterization of alumina electrostatic chuck for silicon wafer processing. *Korus 99: Third Russian-Korean Int. Symp. Sci. Tech.* **1–2**, 532–535 (1999).

32. R. Moser, T. Higuchi, Electrostatic rotation of glass disc. *J. Electrost.* **55**, 97–108 (2002). doi:10.1016/S0304-3886(01)00186-3

33. C. Cabuz, E. I. Cabuz, T. R. Ohnstein, J. Neus, R. Maboudian, Factors enhancing the reliability of touch-mode electrostatic actuators. *Sens. Actuators A Phys.* **79**, 245–250 (2000). doi:10.1016/S0924-4247(99)00281-2

34. R. J. Wood, K. Cho, K. Hoffman, A novel multi-axis force sensor for microrobotics applications. *Smart Mater. Struct.* **18**, 125002 (2009). doi:10.1088/0964-1726/18/12/125002

References and Notes

1. D. Floreano, R. J. Wood, Science, technology and the future of small autonomous drones. *Nature* **521**, 460–466 (2015). Medline doi:10.1038/nature14542

2. M. Tschapka, Pollination of the understorey palm *Calyptrogyne ghiesbreghtiana* by hovering and perching bats. *Biol. J. Linn. Soc. Lond.* **80**, 281–288 (2003). doi:10.1046/j.1095-8312.2003.00235.x

3. B. Anderson, W. W. Cole, S. C. H. Barrett, Botany: Specialized bird perch aids cross-pollination. *Nature* **435**, 41–42 (2005). Medline doi:10.1038/435041a

4. M. Sazima, I. Sazima, The perching bird Coereba flaveola as a co-pollinator of bromeliad flowers in southeastern Brazil. *Can. J. Zool.* **77**, 47–51 (1999). doi:10.1139/cjz-77-1-47

5. C. E. Doyle, J. J. Bird, T. A. Isom, J. C. Kallman, D. F. Bareiss, D. J. Dunlop, R. J. King, J. J. Abbott, M. A. Minor, An avian-inspired passive mechanism for quadrotor perching. *IEEE/ASME Trans. Mechatron.* **18**, 506–517 (2013). doi:10.1109/TMECH.2012.2211081

6. E. W. Hawkes *et al.*, "Dynamic surface grasping with directional adhesion," 2013 IEEE/RSJ International Conference on Intelligent Robots and Systems (IROS), pp. 5487–5493 (2013).

7. J. F. Roberts, J. C. Zufferey, D. Floreano, "Energy management for indoor hovering robots," 2008 IEEE/RSJ International Conference on Intelligent Robots and Systems (IROS), vols 1–3, Conference Proceedings, pp. 1242–1247 (2008).

8. L. Daler, A. Klaptocz, A. Briod, M. Sitti, D. Floreano, "A perching mechanism for flying robots using a fibre-based adhesive," 2013 IEEE International Conference on Robotics and Automation (ICRA), pp. 4433-4438 (2013).

9. D. Mellinger, M. Shomin, V. Kumar, Control of quadrotors for robust perching and landing. *Proc. Int. Power. Lift Conf.* **2010**, 205–225 (2010).

10. M. Kovač, J. Germann, C. Hürzeler, R. Y. Siegwart, D. Floreano, A perching mechanism for micro aerial vehicles. *J. Micro-Nano Mech.* **5**, 77–91 (2009). doi:10.1007/s12213-010-0026-1

11. A. Lussier Desbiens, A. Asbeck, M. Cutkosky, Landing, perching and taking off from vertical surfaces. *Int. J. Robot. Res.* **30**, 355–370 (2011). doi:10.1177/0278364910393286

12. R. Cory, R. Tedrake, Experiments in fixed-wing UAV perching. *Proc. AIAA Guid. Nav. Contr. Conf.* **2008**, 1–12 (2008).

13. A. Frank, J. McGrew, M. Valenti, D. Levine, J. P. How, *Hover, Transition, and Level Flight Control Design for a Single-Propeller Indoor Airplane* (Defense Technical Information Center, 2007).

14. M. L. Anderson *et al.*, "The sticky-pad plane and other innovative concepts for perching uavs," 47th AIAA Aerospace Sciences Meeting (2009).

15. G. J. Monkman, An analysis of astrictive prehension. *Int. J. Robot. Res.* **16**, 1–10 (1997). doi:10.1177/027836499701600101

16. J. P. D. Téllez, J. Krahn, C. Menon, "Characterization of electro-adhesives for robotic applications," 2011 IEEE International Conference on Robotics and Biomimetics (ROBIO), pp. 1867–1872 (2011).

17. H. Prahlad, R. Pelrine, S. Stanford, J. Marlow, R. Kornbluh, "Electroadhesive robots—Wall climbing robots enabled by a novel, robust, and electrically controllable adhesion technology," 2008 IEEE International Conference on Robotics and Automation (ICRA), pp. 3028–3033 (2008).

18. R. Liu, R. Chen, H. Shen, R. Zhang, Wall climbing robot using electrostatic adhesion force generated by flexible interdigital electrodes. *Int. J. Adv. Robot. Syst.* **10**, 36 (2013).

19. R. Chen, R. Liu, H. Shen, "Modeling and analysis of electric field and electrostatic adhesion force generated by interdigital electrodes for wall climbing robots," 2013 IEEE/RSJ International Conference on Intelligent Robots and Systems (IROS), pp. 2327–2332 (2013).

20. H. Wang, A. Yamamoto, T. Higuchi, "Electrostatic-motor-driven electroadhesive robot," 2012 IEEE/RSJ International Conference on Intelligent Robots and Systems (IROS), pp. 914–919 (2012).

21. D. Ruffatto 3rd, A. Parness, M. Spenko, Improving controllable adhesion on both rough and smooth surfaces with a hybrid electrostatic/gecko-like adhesive. *J. R. Soc. Interface* **11**, 20131089 (2014). Medline doi:10.1098/rsif.2013.1089

22. L. Wang, L. Graber, F. Iida, Large-payload climbing in complex vertical environments using thermoplastic adhesive bonds. *IEEE Trans. Robot.* **29**, 863–874 (2013). doi:10.1109/TRO.2013.2256312

23. K. Y. Ma, P. Chirarattananon, S. B. Fuller, R. J. Wood, Controlled flight of a biologically inspired, insect-scale robot. *Science* **340**, 603–607 (2013). Medline doi:10.1126/science.1231806

24. Materials and methods are aviailable as supplementary materials on *Science* Online.

25. M. R. Sogard, A. R. Mikkelson, M. Nataraju, K. T. Turner, R. L. Engelstad, Analysis of Coulomb and Johnsen-Rahbek electrostatic chuck performance for extreme ultraviolet lithography. *J. Vac. Sci. Technol. B* **25**, 2155–2161 (2007). doi:10.1116/1.2798724

26. E. Baird, N. Boeddeker, M. R. Ibbotson, M. V. Srinivasan, A universal strategy for visually guided landing. *Proc. Natl. Acad. Sci. U.S.A.* **110**, 18686–18691 (2013). Medline doi:10.1073/pnas.1314311110

27. J. Germann, B. Schubert, D. Floreano, "Stretchable electroadhesion for soft robots," 2014 IEEE/RSJ International Conference on Intelligent Robots and Systems (IROS), pp. 3933–3938 (2014).

28. G. Kalkowski, S. Risse, V. Guyenot, Electrostatic chuck behaviour at ambient conditions. *Microelectron. Eng.* **61-62**, 357–361 (2002). doi:10.1016/S0167-9317(02)00501-4

29. J. van Elp, P. T. M. Giesen, A. M. M. de Groof, Low-thermal expansion electrostatic chuck materials and clamp mechanisms in vacuum and air. *Microelectron. Eng.* **73-74**, 941–947 (2004). doi:10.1016/S0167-9317(04)00248-5

30. M. Karpelson, J. P. Whitney, G. Y. Wei, R. J. Wood, Design and fabrication of ultralight high-voltage power circuits for flapping-wing robotic insects. *Appl. Power Electron. Conf.* **2011**, 2070–2077 (2011).

31. K. J. Jeong, S. Spoutai, S. H. Choi, T. Y. Cho, H. G. Chun, A study on the fabrication and characterization of alumina electrostatic chuck for silicon wafer processing. *Korus 99: Third Russian-Korean Int. Symp. Sci. Tech.* **1–2**, 532–535 (1999).

32. R. Moser, T. Higuchi, Electrostatic rotation of glass disc. *J. Electrost.* **55**, 97–108 (2002). doi:10.1016/S0304-3886(01)00186-3

33. C. Cabuz, E. I. Cabuz, T. R. Ohnstein, J. Neus, R. Maboudian, Factors enhancing the reliability of touch-mode electrostatic actuators. *Sens. Actuators A Phys.* **79**, 245–250 (2000). doi:10.1016/S0924-4247(99)00281-2

34. R. J. Wood, K. Cho, K. Hoffman, A novel multi-axis force sensor for microrobotics applications. *Smart Mater. Struct.* **18**, 125002 (2009). doi:10.1088/0964-1726/18/12/125002